Nonlinear propagation dynamics of finite-energy Airy beams

P. Panagiotopoulos,[1,*] D. Abdollahpour,[1] A. Lotti,[2,3] A. Couairon,[2] D. Faccio,[3,4] D. G. Papazoglou,[1,5] and S. Tzortzakis[1,5]

[1]*Institute of Electronic Structure and Laser, Foundation for Research and Technology Hellas, P.O. Box 1527, 71110 Heraklion, Greece*

[2]*Centre de Physique Théorique, École Polytechnique, CNRS, F-91128 Palaiseau, France*

[3]*CNISM and Department of Physics and Mathematics, Università dell'Insubria, I-22100 Como, Italy*

[4]*School of Engineering and Physical Sciences, SUPA, Heriot-Watt University, Edinburgh EH14 4AS, United Kingdom*

[5]*Materials Science and Technology Department, University of Crete, P.O. Box 2208, 71003 Heraklion, Greece*

(Received 17 November 2011; published 27 July 2012)

The nonlinear dynamics of intense truncated Airy beams in Kerr ionizing media are investigated from numerical simulations and experiments. We show numerically that a competition between the linear and nonlinear effects takes place and may be modified by tuning the width of the main lobe of the Airy beam and the size of the truncating diaphragm. Our analysis shows that the acceleration of the Airy peak, an inherent feature of linear Airy beam propagation, is preserved only for powers in the main Airy lobe below a certain threshold. Nonlinear propagation of intense Airy beams with low power in the main lobe is sustained by a continuous energy flux from its neighbors, similarly to the mechanism sustaining nonlinear Bessel beam propagation. Airy beams with higher powers in the main lobe are reshaped into a multifilamentary pattern induced by Kerr and multiphoton nonlinearities. The nucleation of new filaments and their interaction affect the acceleration of the main Airy lobes. We finally show that the size of the truncation constitutes a control parameter for the energy flux that features the Airy beam acceleration. Experiments performed in water corroborate the existence of these two distinct nonlinear propagation regimes.

DOI: 10.1103/PhysRevA.86.013842 PACS number(s): 42.25.−p, 42.65.Jx, 42.65.Sf

I. INTRODUCTION

Airy beams with finite energy were recently proposed as genuine nonspreading optical waves [1,2]. Airy beams are intrinsically one-dimensional structures [3], but several combinations were demonstrated since 2007 for realizing a two- or three-dimensional nonspreading optical wave packet by linear superposition of subdimensional nonspreading structures [4–6]. In 2010, Chong *et al.* generated Bessel-Airy beams consisting of a Bessel beam in the transverse plane and an Airy distribution along the longitudinal dimension [7]. Abdollahpour *et al.* generated three-dimensional (3D) Airy light bullets consisting of an Airy beam profile in each dimension [8]. Nonlinear generation techniques were also used; for example, by Ellenbogen *et al.* who generated Airy beams at the second harmonic of a pump beam by using nonlinear three-wave mixing in nonlinear crystals [9].

In the linear regime the propagation dynamics of Airy beams has been studied extensively. The two most exotic features of Airy beams (namely, self-healing and transverse acceleration) have been investigated by Broky *et al.* [10] and Siviloglou *et al.* [11]. The dependence of Airy wave packets on wavelength, spatial coherence and dispersion have been investigated in Refs. [12,13]. One of the interests of these structures is their potential for applications in extreme nonlinear optics. Airy beams in the nonlinear regime were discussed in Refs. [8,14–16] from the observation of spectacular manifestations common with the nonlinear dynamics of light filaments, such as supercontinuum generation and conical emission. Lotti *et al.* recently discovered the existence of stationary nonlinear Airy beams in one transverse dimension [17]. An open question concerns the properties of multidimensional Airy beams in the nonlinear regime. High-intensity Airy beams propagating in a gas or a transparent medium can be strongly affected by nonlinear effects that play a key role in the dynamics of ultrashort laser pulse propagation (i.e., the optical Kerr effect, multiphoton absorption and ionization to cite only a few [18–20]).

In this paper we investigate the propagation dynamics of intense Airy beams with particular emphasis on the competition between the features of linear Airy beam propagation (acceleration property, stationarity) and the trend of the most intense lobes of an Airy beam to behave as filaments. We identify nonlinear propagation regimes of intense Airy beams in a Kerr medium by means of numerical simulations, with special attention paid to beam transverse acceleration and stationarity. We notably answer to the following questions: Is the Airy beam profile affected by nonlinear propagation or by finite size effects? Does the trajectory and transverse acceleration of the most intense peak of an Airy beam depend on its power content?

II. PROPAGATION MODEL

A. Linear Airy beam propagation

The propagation of the finite-energy Airy beam (FEAB) introduced by Siviloglou and Christodoulides [1,2] is governed by the paraxial equation

$$\frac{\partial E}{\partial z} = \frac{i}{2k}\Delta_\perp E, \tag{1}$$

where $\Delta_\perp$ denotes the Laplacian in the transverse diffraction plane and k denotes the propagation constant. Equation (1) describes the evolution of the envelope of the electric field of a quasimonochromatic beam ($\Delta\lambda/\lambda \ll 1$) in a dispersionless medium along the propagation axis z in the linear regime

*parisps@iesl.forth.gr

(i.e., due to diffraction effects). It is directly derived from the Maxwell equations for a material without magnetization and no free charges and currents, by applying the paraxial approximation (wavelength much shorter than beam waist: $\lambda_0 \ll w_0$) and the slowly varying envelope approximation (wavelength much shorter than typical evolution distance for the beam envelope: $\lambda_0 \ll z_0$, where $z_0 \equiv k w_0^2/2$ denotes the diffraction length of a beam of waist w_0) [18].

In one transverse dimension x, the propagation of the FEAB

$$E\,(z=0,x) = E_0 \mathrm{Ai}\,(x/w_0)\exp\,(ax/w_0)\,, \tag{2}$$

where Ai denotes the Airy function and w_0 denotes the width of the central lobe, is described by

$$E(z,x) = E_0 \mathrm{Ai}(s-\zeta^2 + i2a\zeta)\exp[a(s-2\zeta^2)] \times \exp[i\zeta(-2\zeta^2/3 + a^2 + s)], \tag{3}$$

where $s = x/w_0$ and $\zeta = z/(4z_0)$ are the normalized transverse coordinate and propagation distance respectively. Transverse acceleration of the peak intensity of Airy beams is one of their peculiar properties. From Eq. (3), this acceleration obey $s - \zeta^2 = s_0$; that is, in physical units,

$$x = x_0 + \frac{z^2}{4k^2 w_0^3}, \tag{4}$$

where x_0 denotes the initial position of the peak at $z = 0$. Equation (4) shows that the Airy beam follows a parabolic trajectory $x = x_0 + z^2/(2r_c)$ with curvature radius $r_c = 2k^2 w_0^3$. The typical propagation distance for the peak of the Airy beam to translate by w_0 is $4z_0$. In addition, the peak intensity of the Airy beam should vary as $\exp(-az^2/4z_0^2)$; that is, the length over which the intensity of the FEAB is larger than half the maximum value due to finite size effects is

$$z_A = 4z_0\sqrt{\ln(2)/a}. \tag{5}$$

By analogy with the Bessel zone for Bessel beams, we will call this quantity the Airy zone. The FEAB given by Eq. (3) extends to two transverse dimensions (x,y) by a superposition of two one-dimensional (1D) FEABs: in this case, its acceleration in the y-z plane is characterized by the same curvature $y = y_0 + z^2/(2r_c)$, where y_0 denotes the initial position of the peak at $z = 0$.

B. Nonlinear Airy beam propagation

The propagation of a quasimonochromatic laser beam in the nonlinear regime is described by a scalar equation of nonlinear Schrödinger type, which is obtained by applying, as in Eq. (1), the paraxial and slowly varying envelope approximations while using the reference frame of the pulse $[z, t = t_{\mathrm{lab}} - z/v_g(\omega_0)]$ where $v_g(\omega_0) \equiv \partial\omega/\partial k\,|_{\omega_0}$ denotes the group velocity [19]:

$$\frac{\partial E}{\partial z} = \frac{i}{2k}\Delta_\perp E + i\frac{\omega_0}{c}n_2|E|^2E - \frac{\beta_K}{2}|E|^{2K-2}E - i\frac{\omega_0}{n_0 c}\frac{\rho}{2\rho_c}E. \tag{6}$$

The second term on the right-hand side of Eq. (6) accounts for the optical Kerr effect with coefficient n_2. The remaining terms describe multiphoton absorption (MPA) with coefficient β_K (i.e., the energy losses necessary to ionize the medium) and plasma defocusing by the electron plasma of density ρ generated by multiphoton ionization, with $\rho_c = 1.7 \times 10^{21}$ cm^{-3} being the critical density beyond which the plasma becomes opaque at 800 nm.

Multiphoton ionization (MPI) is described by the evolution equation for the electron density:

$$\frac{\partial \rho}{\partial t} = \sigma_K |E\,(t)\,|^{2K}\,(\rho_{nt} - \rho)\,, \tag{7}$$

where the coefficients σ_K for multiphoton ionization and β_K for MPA are linked through the relation $\beta_K = K\hbar\omega_0\rho_{nt}\sigma_K$. Multiphoton processes involve a number of photons $K \equiv \langle U_i/\hbar\omega_0\rangle + 1$, where U_i denotes the ionization potential and ρ_{nt} denotes the density of neutral molecules.

For simulations in air, we used the parameters $n_2 = 3.2 \times 10^{-19}$ cm^2/W associated with a critical power for self-focusing of $P_{cr} = 3$ GW at the laser wavelength of 800 nm [21,22]. The coefficients for MPI and MPA, $\sigma_8 = 4 \times 10^{-96}$ s^{-1} cm^{16}/W^8 and $\beta_8 = 4 \times 10^{-95}$ cm^{13}/W^7, were calculated from the Keldysh formulation taken in the multiphoton limit [23], revisited by Ilkov *et al.* [24], with detailed formulas given in Ref. [18] using $U_i = 12.06$ eV, $K = 8$ photons, and $\rho_{nt} = 5 \times 10^{18}$ cm^{-3} for oxygen molecules.

For simulations in water, we used the parameters $n_2 = 1.6 \times 10^{-16}$ cm^2/W, $P_{cr} = 4$ MW [25,26], $K = 5$ photons, $\sigma_K = 1 \times 10^{-54}$ s^{-1} cm^{10}/W^5, $\beta_K = 8.3 \times 10^{-50}$ cm^7/W^4 [26,27], $\rho_{nt} = 6.6 \times 10^{22}$ cm^{-3} [28], and $n_0 = 1.33$.

C. Validity of model approximations

The goal of this work is to describe the spatial dynamics of nonlinear Airy beams. In our experiments presented below, we used femtosecond laser pulses with $t_p = 35$ fs nominal duration propagating in air or passing through various optical elements to generate an Airy beam which results in 80 fs pulses propagating further in water. We assumed that the laser pulse profile remains undistorted along the propagation; that is, we considered that effects associated with changes in the temporal profile are sufficiently weak (or slow) with respect to the spatial effects induced by self-focusing, plasma defocusing, and multiphoton absorption. This approximation requires justification to guarantee the validity of our model (6) to describe the spatial dynamics of propagating nonlinear pulses. This is the goal of this section, where we evaluate the importance of temporal effects by comparing their characteristic lengths.

Taking into account the material parameters, we evaluated the nonlinear lengths $L_{\mathrm{Kerr}} = c/(\omega_0 n_2 I)$, $L_{\mathrm{MPA}} = 1/(2\beta_K I^{K-1})$, and $L_{\mathrm{Plasma}} = 2/(\sigma\omega_0\rho\tau)$ [29] of the Airy beams used in this work and compared them to the dispersive length of our laser pulse. Since both lengths are a function of the local intensity, they generally vary along z. For propagation in air, the dispersive length of the pulse is $L_{\mathrm{GVD}} = t_p^2/(2k_0'') \sim 30.6$ m, for a dispersive coefficient $k_0'' = 0.2$ fs^2/cm, whereas at their minimum value both nonlinear characteristic lengths decrease down to about 1.6 cm (Kerr) and 0.4 cm (MPA). This is three order of magnitude shorter that L_{GVD}. Comparison of these lengths justify that the effect of dispersion can be safely neglected compared to nonlinear effects.

For the Airy beams propagating in water, the nonlinear lengths are as short as $L_{\mathrm{Kerr}} \sim 110\ \mu$m and $L_{\mathrm{MPA}} \sim 76\ \mu$m at

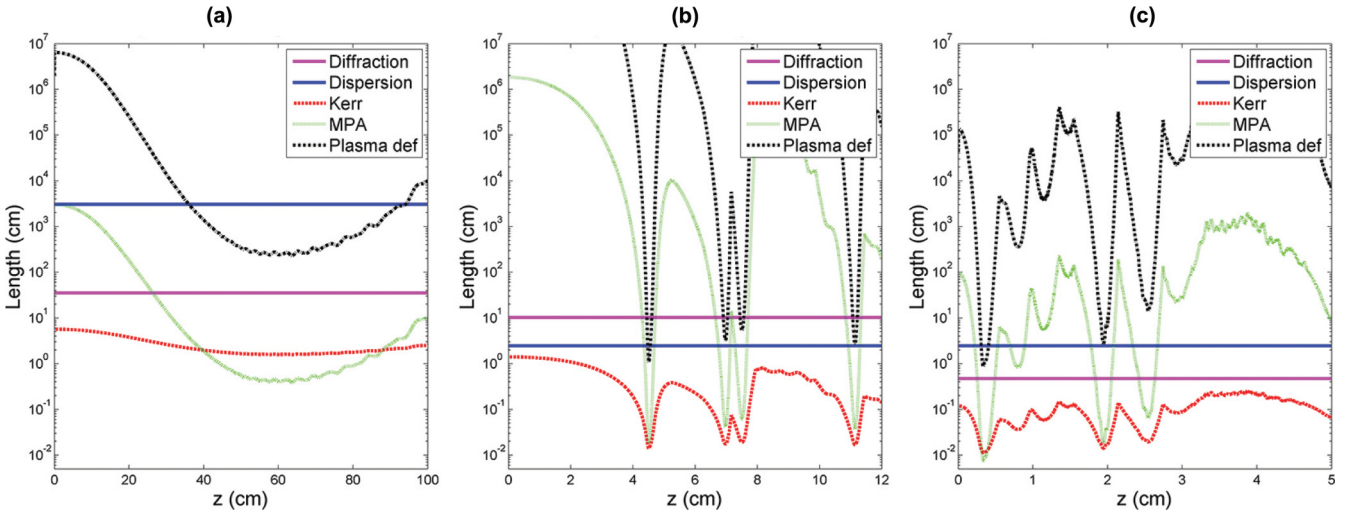

FIG. 1. (Color online) Logscale plot of the characteristic lengths of physical effects vs propagation distance for (a) the Airy beam of Fig. 3(c) propagating in air, (b) the Airy beam of Fig. 11 propagating in water, and (c) the Airy beam of figure Fig. 12 propagating in water. The blue and magenta continuous lines that correspond to the characteristic lengths of dispersion and diffraction respectively. Green dotted line is for MPA, red dashed line is for Kerr, and black dash-dotted line is for plasma defocusing.

their minimum, both much shorter than the dispersive length $L_{\mathrm{GVD}} = 2.47$ cm, for a dispersive coefficient $k_0'' = 248\ \mathrm{fs}^2/\mathrm{cm}$ [30]. This means that, despite the high dispersion of water, we can still neglect it since the nonlinear effects are much stronger in the high-intensity regime.

Figure 1 shows the characteristic lengths for the three main cases (one Airy beam propagating in air and two others in water) in this work along propagation distance. In addition Table I is showing the analytical formulas for all characteristic lengths used for the calculations of the curves in Fig. 1, and the values that give the minimum for each physical effect.

Dispersion effectively broadens the pulse even in the linear propagation regime, although neglected in Eq. (6), but for our parameters it has a homogeneous effect on the whole beam which does not seriously affect the much faster spatial dynamics. The laser pulse profile can therefore be safely assumed to remain undistorted along propagation. We used this undistorted profile to calculate the generated plasma density by means of Eq. (7), where ionization rate depends on the local intensity. The electron density used in the plasma defocusing term in Eq. (6) is evaluated at the central local time $t = 0$ after calculation by Eq. (6).

Our model includes another approximation: we considered multiphoton ionization of a single species in air (i.e., oxygen) with the lowest ionization potential $U_i = 12.06$ eV. This is usually an excellent approximation in the regime of ultrashort laser pulse filamentation since a more complete model taking into account ionization of both oxygen and nitrogen molecules gives a negligible additional contribution to the electron density due the much smaller ionization rate of nitrogen compared to oxygen molecules [31].

The above evaluation of dispersive lengths justifies this assumption and the use of Eq. (6) [19]. We emphasize that assuming the spatial profile is mainly shaped by spatial dynamics (diffraction, self-focusing, multiphoton absorption, and plasma defocusing) and neglecting the effect of the much weaker temporal dynamics on the beam shape will be further justified by the good agreement between simulation and results and measurements of nonlinear Airy beam profiles.

TABLE I. Minimum characteristic lengths of physical effects.

		Concerning Fig. 3(c)		Concerning Fig. 11		Concerning Fig. 12	
Physical effect	Length formula	Position of minimum L	min[L] (cm)	Position of minimum L	min[L] (cm)	Position of minimum L	min[L] (cm)
Kerr	$L_{\mathrm{Kerr}} = \frac{c}{(\omega_0 n_2 I)}$	$I = I_{\max} = 2.5 \times 10^{13}$ W/cm^2	1.6	$I = I_{\max} = 4.2 \times 10^{12}$ W/cm^2	1.4×10^{-2}	$I = I_{\max} = 5.3 \times 10^{12}$ W/cm^2	1.1×10^{-2}
MPA	$L_{\mathrm{MPA}} = \frac{1}{(2\beta_K I^{K-1})}$	$I = I_{\max}$	0.4	$I = I_{\max}$	1.9×10^{-2}	$I = I_{\max}$	7.6×10^{-3}
Plasma defocusing	$L_{\mathrm{Plasma}} = \frac{2}{(\sigma\omega_0\rho\tau)}$	$\rho = \rho_{\max} = 1.9 \times 10^{16}$ cm^{-3}	2.3×10^2	$\rho = \rho_{\max} = 3.2 \times 10^{18}$ cm^{-3}	1.0	$\rho = \rho_{\max} = 3.9 \times 10^{18}$ cm^{-3}	0.9
Dispersion	$L_{\mathrm{GVD}} = \frac{t_p^2}{2k_0''}$	$t_p = 35$ fs	3.1×10^3	$t_p = 35$ fs	2.47	$t_p = 35$ fs	2.47
Diffraction	$L_{\mathrm{Diff}} = \frac{k_0 R_0^2}{2}$	$R_0 = w_0 = 300\ \mu$m	35	$R_0 = w_0 = 140\ \mu$m	10	$R_0 = w_0 = 30\ \mu$m	0.47 0.47

D. Initial condition: Truncated Airy beam

Our simulations start from an already formed Airy beam described by

$$E\,(z=0,x,y) = E_0 \mathrm{Ai}\,(x/w_0)\,\mathrm{Ai}\,(y/w_0)\,T\,(x,y)\,, \qquad (8)$$

where T mimics the effect of a circular diaphragm which truncates the Airy beam and transforms it into a FEAB: $T(x,y)=1$ if $r \equiv \sqrt{x^2+y^2} < r_d$ and $T(x,y)=0$ if $r \geqslant r_d$. This input condition constitutes a two-dimensional FEAB similar to Eq. (2), as if it was generated in vacuum; for example, by methods described in Refs. [2,4] and entered in the nonlinear medium (air) from the focus. With air, this can be achieved with the setup proposed by Diels *et al.* [32]. By placing the circular diaphragm at the focal point we truncate the already formed wide Airy beam to the desired size without influencing the shape of the inner lobes. The position immediately after the circular diaphragm is the initial state for the simulation. This is analogous to linearly focusing a beam on the entrance face of a sample and investigating the subsequent nonlinear dynamics [33]. The corresponding laser pulse is assumed to be Gaussian with full width at half maximum of 35 fs and to remain undistorted (frozen time). We consider Airy beams with initial peak intensity $I_0 = 7\times10^{12}$ W/cm^2 and different lobe widths $w_0 = 100$ μm, $w_0 = 200$ μm, and $w_0 = 300$ μm.

Widening the main lobe width while keeping the input intensity $I_0 \equiv |E_0|^2$ constant is effectively increasing the power content of the main lobe, P_A, which is evaluated as the power in the quadrant of the (x,y) plane delimited by the first zero of the Airy function:

$$P_= \int_{u_0 w_0}^{+\infty}\int_{u_0 w_0}^{+\infty} |E\,(x,y)\,|^2 dxdy = I_0\,(w_0 f)^2\,, \qquad (9)$$

where $f = m^{-2}\int_{u_0}^{+\infty} Ai^2(u)du = 1.71$, $u_0 = -2.34$ denotes the first zero position, and $m \sim 0.54$ denotes the maximum of the Airy function. The three chosen lobe widths correspond to powers $P_A = 2$ GW (0.65 P_{cr}), $P_A = 8$ GW (2.6 P_{cr}), and $P_A = 18$ GW (5.8 P_{cr}). The critical power for self-focusing and the ratio P/P_{cr}, where P denotes the total beam power, usually constitutes a reference for evaluating the potential of a Gaussian beam for self-focusing at powers slightly exceeding P_{cr}, or breaking up into multiple filaments at higher powers. For Airy beams, the main lobe power P_A is a much better indicator than the total power in the Airy beam for characterizing self-focusing of the main lobe since P strongly depends on the truncation size whereas P_A does not, except in extreme situations that no longer correspond to an Airy beam. Using P_A also allows us to consider P_{cr} as an estimate for the self-focusing threshold even if the main Airy lobe is not Gaussian. For the three powers considered above, P_A exceeds P_{cr} for the Airy beams with $w_0 = 200$ μm and 300 μm, which are thus expected to self-focus and collapse upon themselves. Higher powers are actually required in order to clearly observe self-focusing. We compare nonlinear propagation of the three intense Airy beams defined above, hereafter called Airy beams with moderate powers, with that of high power Airy beams having the same peak intensity and width but a tenfold increase of the ratio P_A/P_{cr}.

III. PROPAGATION OF INTENSE AIRY BEAMS IN WEAKLY NONLINEAR REGIME

Figure 2 shows cross sections of intense Airy beams at different propagation distances during their nonlinear propagation. For the three cases displayed in columns $w_0 = 100$, 200, and 300 μm, the radius of the circular diaphragm is $r_d = 4.5$ mm. Propagation distances increase from top to bottom from $z = 0$ up to $z = 80$ cm with 20 cm steps. The last row of Fig. 2 shows the beam profiles that would be obtained for a linear propagation over 80 cm of each input Airy beam with the same w_0. The intense peak of the Airy beam accelerates transversely faster when the initial size of the central lobe is small. At a propagation distance of 80 cm, the peak of the Airy beam with $w_0 = 100$ μm (first column in Fig. 2) reached the position $x = y \sim 2.5$ mm, whereas the peaks of the Airy beams with $w_0 = 200$ and $w_0 = 300$ μm (second and third column in Fig. 2) show a slower transverse acceleration by a factor of 8 and 27, respectively. It is readily seen in the third column in Fig. 2 that the Airy beam with the largest lobe remains nearly in place but undergoes self-focusing. The effect of self-focusing on the Airy lobes is also clear from the comparison of the beam cross sections after nonlinear and linear propagation over 80 cm, shown in the last two rows of Fig. 2. For the same input intensity, the main lobe of the Airy beam carrying the highest power ($w_0 = 300$ μm, third column of Fig. 2) shrinks faster than that of the less-powerful Airy beams. Even the secondary lobes of the most powerful Airy beam are significantly reshaped. This trend to self-focus due to the Kerr effect competes with the acceleration of the Airy beam inherited from the properties of linearly propagating Airy beams. Both processes can be viewed as a transfer of power: the acceleration corresponds to a transfer from the secondary lobes to the main lobe and is responsible for the self-healing property of Airy beams [34], whereas self-focusing concentrates the power of a given lobe upon itself.

The left column of Fig. 3 shows a comparison of the peak intensity and generated plasma density during the nonlinear propagation of the three Airy beams with moderate powers. In these cases, for each propagation distance, intensities and electron densities reported in Fig. 3 correspond to different positions x,y of the peak of the Airy beam because it is turning. However, as shown in Fig. 2, the initial main lobe remains the most intense all along the propagation distance and the reported electron densities in Fig. 3 are generated by that lobe. The right column of Fig. 3 shows isointensity surfaces for the three cases, plotted in the (x,y,z) space (central time slice $t = 0$). It can be readily seen that, in these cases, in spite of high intensities and nonlinear effects, the main and the secondary lobes follow the parabolic trajectory which would characterize the linear propagation of the input Airy beam.

Airy beams with $w_0 = 200$ μm and 300 μm have $P_A/P_{cr} > 1$. Thus if the most intense Airy lobe behaved like a typical Gaussian beam, it would self-focus and collapse upon itself under the nonlinear action of the optical Kerr effect. Then collapse would be arrested by multiphoton absorption, plasma generation, and plasma defocusing as in ultrashort pulse filamentation. Since these phenomena are high-order processes, they should lead to saturation and prevent intensity

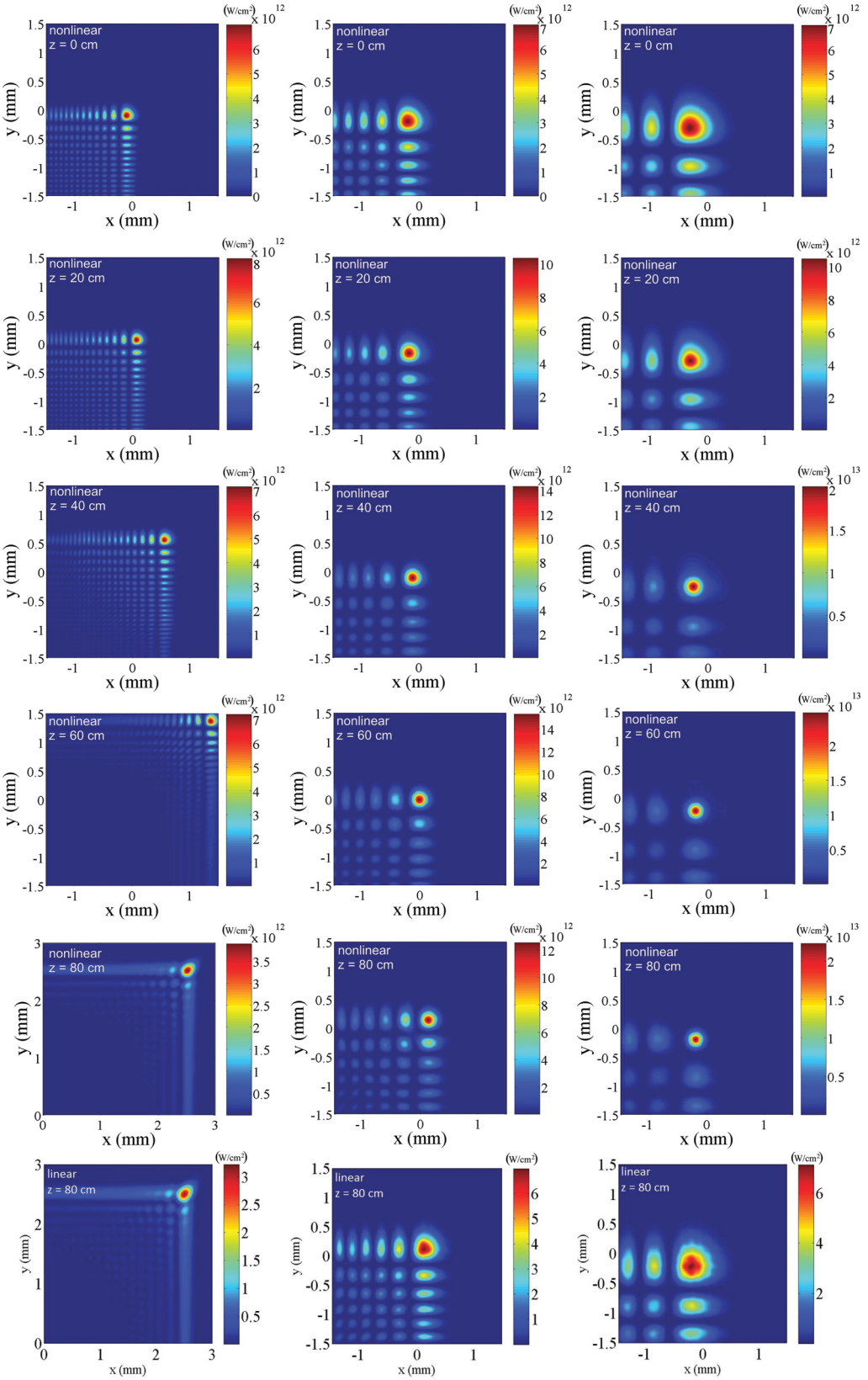

FIG. 2. (Color online) (x,y) intensity plots of nonlinear Airy beams with initial peak intensity 7×10^{12} W/cm^2 and different central lobe size. First column is for $w_0 = 100$ μm, second column is for $w_0 = 200$ μm, and third column is for $w_0 = 300$ μm. The propagation distance varies from $z = 0$ (first line) to $z = 80$ cm (fifth line) by steps of 20 cm. The diaphragm radius for all cases is $r_d = 4.5$ mm. The last line shows the beam profiles after linear propagation of the three Airy beams over $z = 80$ cm. Note the larger window used for plotting the cross section in the bottom-left corner.

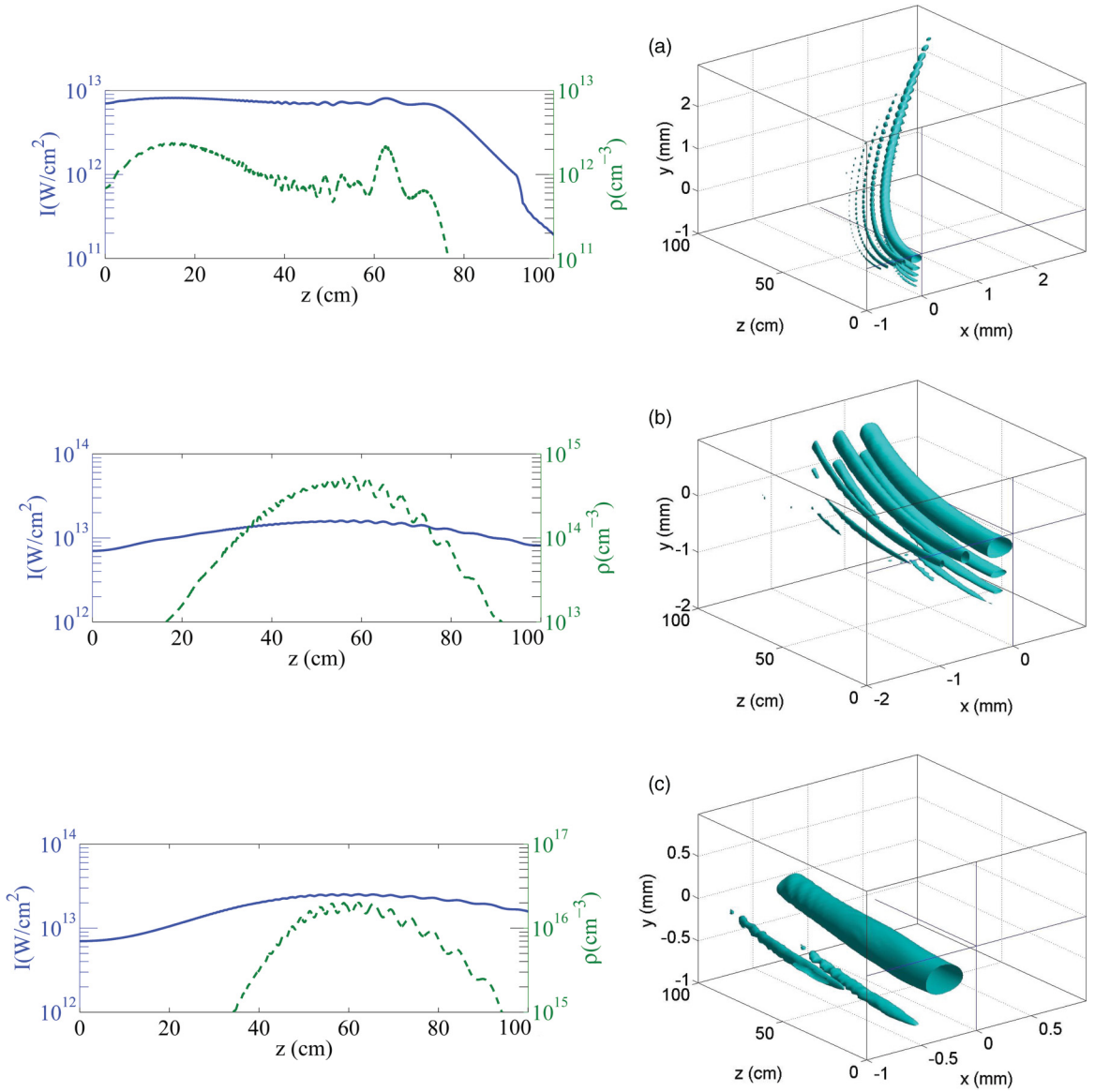

FIG. 3. (Color online) Nonlinear propagation of intense Airy beams with initial central lobe width of 100 μm (first line), 200 μm (second line), and 300 μm (third line). Left column is peak intensity (continuous curve, left axis), electron density (dashed curve, right axis). Right column is for isosurfaces of the intensity distribution showing the trajectories of the main and secondary lobes of the Airy beam. The axes crossing at the origin are a guide for the eye so as to evaluate the curvature radius of the main peak trajectory. Note the different box sizes.

to grow above a certain value which can be predicted by simple estimations [35,36]. However, our simulations show a different behavior that is more similar to that of Bessel filaments [33,37]. First, no obvious nonlinear focus of the main Airy lobe appears even though we considered propagation distances much larger than the collapse distance estimated from Marburger's formula for Gaussian beams with the same widths and powers as the considered Airy beams (i.e., 7.7 and 8.4 cm for the beams with 200 μm, $2.6P_{cr}$ and 300 μm, $5.8P_{cr}$, respectively). Second, for the widest Airy beams with width of 200 μm [Fig. 3(b)] and 300 μm [Fig. 3(c)], the peak intensity reaches values up to 2×10^{13} W/cm^2 and the electron density exceeds 10^{16} cm^{-3} but no plateau is obtained indicating the absence of a saturation process of the same nature as in filamentation [36]. The intensity profile plotted in Fig. 3(a) does exhibit a plateau over several tens of centimeters but it corresponds to the smallest Airy beam with width of 100 μm [Fig. 3(a)], the power of which is below threshold. Its peak intensity is lower than 10^{13} W/cm^2 and also lower than for a standard filament in air; the electron density of the generated plasma does not exceed a few 10^{12} cm^{-3}, indicating a weakly nonlinear propagation of the Airy beam. The lack of a clear nonlinear focus as well as the absence of intensity plateau in the nonlinear regime suggest that the propagation dynamics of nonlinear Airy beams are governed by the same principles that apply to Bessel filaments.

The intensity profile is well explained by finite size effects: If the Airy beam was infinitely wide, an energy flux from the tail carrying infinite energy would push the main lobe along the diagonal $x = y$ and could sustain its intensity over extended

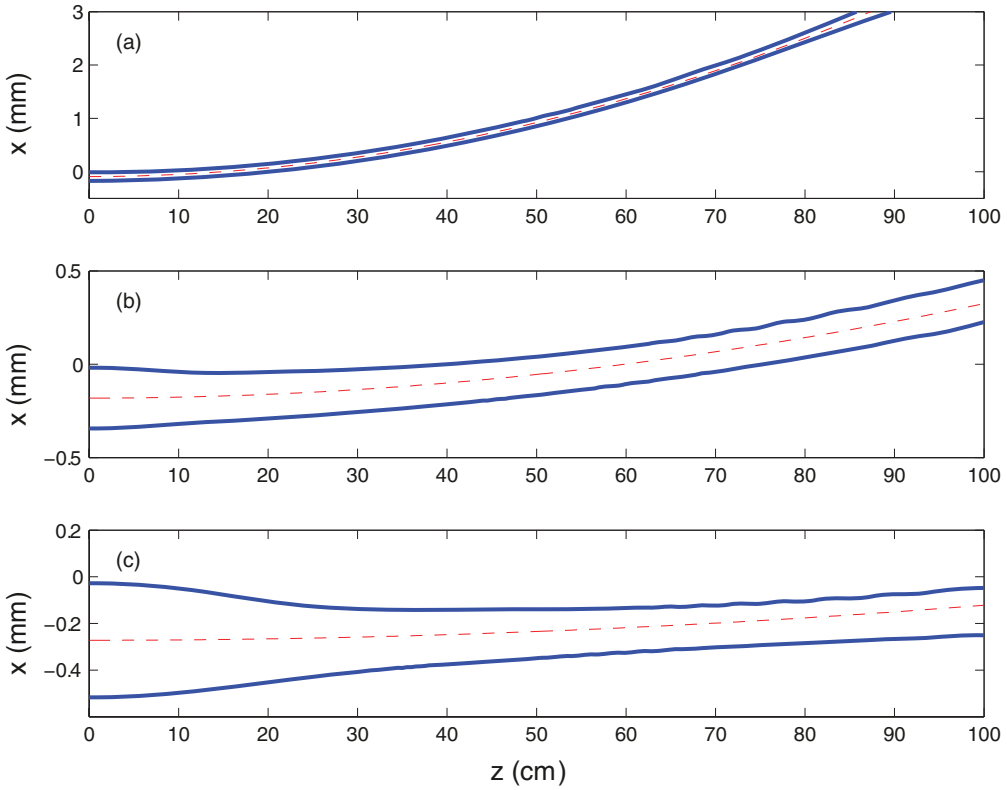

FIG. 4. (Color online) Projection of main lobe trajectory and FWHM of Airy beam along the x direction. (a) Input Airy beam with $w_0 = 100\ \mu$m. (b) Input Airy beam with $w_0 = 200\ \mu$m. (c) Input Airy beam with $w_0 = 300\ \mu$m.

distances exactly as in the case of Bessel beams [37]. With finite energy, the profile of the peak intensity of a *linearly propagating* Airy beam is known to be governed by finite-size effects and should decrease as $\exp[-az^2/(k^2w_0^4)]$ according to Eq. (3) (i.e., faster for large Airy beam lobes). This is the behavior we observe in the nonlinear regime [second stage of propagation in Figs. 3(b) and 3(c)], in conjunction with an initial self-focusing stage that prevails at the beginning of the propagation.

At moderate powers, Airy beams are intense enough to undergo Kerr self-focusing and induce multiphoton absorption; however, the trajectory of the main lobe obtained in the linear regime is preserved in the three cases shown in Fig. 3. The parabolic trajectory of the Airy beam with the smallest lobe width [Fig. 3(a)] exhibits the smallest curvature radius. Figure 4 shows the projection of the main lobe trajectory in the (x,z) plane and its full width at half maximum (FWHM) diameter. The peak clearly turns as a linear Airy beam would do, following a parabolic trajectory that coincides with that given by Eq. (4) (dashed curves in Fig. 4). For the wider input Airy beams [Figs. 3(b), 3(c) and 4(b), 4(c)] the nonlinear propagation starts by a Kerr-induced self-focusing stage with a decrease of the FWHM diameter from $z = 0$ cm to $z = 30$ cm. This indicates a competition between Kerr self-focusing and the acceleration of the Airy beam. From this observation, we identified two situations for which the transverse acceleration of the Airy peak is modified by the nonlinear propagation: (i) higher-power Airy beams and (ii) narrower Airy beam truncation.

IV. PROPAGATION OF INTENSE AIRY BEAMS IN STRONGLY NONLINEAR REGIME

The Airy peak acceleration is quenched when the power of the main lobe is large enough so that self-focusing of the most intense Airy lobe prevails over the peak acceleration. Increasing the width of the main lobe at constant input intensity does increase its power content; however, it simultaneously increases the curvature radius of the Airy beam trajectory, thus requiring a longer propagation distance to see the effect of acceleration quenching. Increasing the input intensity while keeping the width of the main lobe constant results in intensities approaching 10^{13} W/cm^2, which ionize air sufficiently to produce a plasma responsible for a defocusing effect. This leads to an immediate decrease rather than an increase of the intensity in the early stage of propagation. In order to demonstrate the effect of acceleration quenching with a high-power Airy beam having narrow lobes so as to keep propagation distances smaller than 1 m, we arbitrarily increased the Kerr index coefficient by a factor of 10 and used the same input Airy beams as in Sec. III. This keeps the curvature radius of the trajectories of the linearly propagating Airy beams unchanged but increases P_A/P_{cr} by a factor of 10 and allows us to isolate the effect of self-focusing on the beam shape from other nonlinearities, like multiphoton absorption and plasma defocusing. This mimics to some extent an experimental situation in which an Airy beam is formed in vacuum and enters a gas chamber containing pressurized air at 10 atm. Due to the rescaling properties of Eq. (6), the results also represent the propagation of an

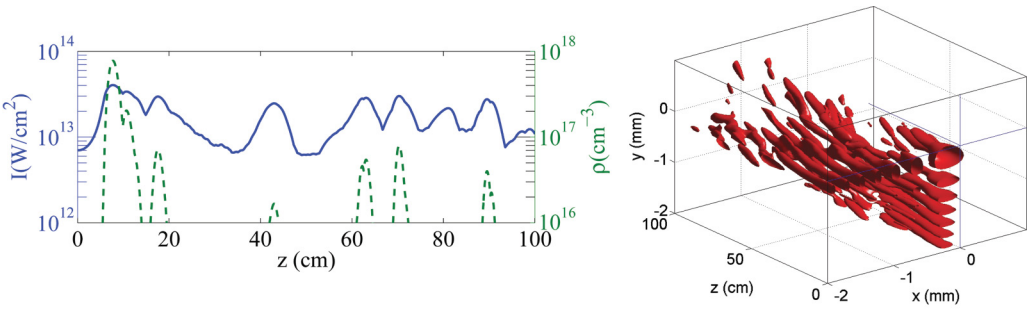

FIG. 5. (Color online) Nonlinear propagation of intense Airy beams with initial central lobe width of 200 μm, $I_0 = 7 \times 10^{12}$ W/cm^2 in a highly nonlinear Kerr medium with $n_2 = 3.2 \times 10^{-18}$ cm^2/W. First line is for peak intensity (continuous curve, left axis), electron density (dashed curve, right axis). Second line is for isosurfaces of the intensity distribution.

input Airy beam with $w_0 = 93$ μm, $I_0 = 1.4 \times 10^{12}$ W/cm^2 generated with an infrared (1500 nm), 130 fs pulse, in water (gap $U_i = 6.5$ eV, same number of photons $K = 8$ in multiphoton processes at 1500 nm, $n_2 = 2 \times 10^{-16}$ cm^2/W, $\rho_{nt} = 6.7 \times 10^{22}$ cm^{-3}, $\beta_K = 2 \times 10^{-89}$ cm^{13}/W^7, and $\sigma_K = 3 \times 10^{-94}$ s^{-1}cm^{16}/W^8). There are many other combinations of beam or pulse parameters ensuring that, for water, the ratios $L_{\text{Kerr}}/L_{\text{Diff}}$, $L_{\text{MPA}}/L_{\text{Diff}}$, and $L_{\text{Plasma}}/L_{\text{Diff}}$ are equal to their counterparts in air at 10 atm.

Figure 5 shows the results of this numerical experiment: The peak intensity displayed on the first line exhibits several cusps which indicate the distances where the intensity of the most intense lobe is decreasing below the intensity of a secondary lobe, which in turn becomes the most intense. Correspondingly, each dashed curve indicates the electron density generated by the most intense peak as a function of propagation distance. Except at the beginning, this electron density is obtained for a different lobe of the Airy beam, which was initially not the most intense. This competition between the different-intensity lobes is illustrated on the isointensity plot shown on the second column of Fig. 5. A general trend of the intensity peaks to follow curved trajectories is observed; however, the initial main lobe clearly undergoes self-focusing over a much shorter distance and disappears after 15 cm. Then the most intense peak is located in a secondary lobe which, after some propagation distance, also disappears. This dynamical process repeats itself until the power in the whole beam is exhausted. The trajectory of the most intense lobe is therefore discontinuous each time a different secondary lobe becomes dominant. The competition between the main and secondary lobes can be followed on the $I(x,y)$ cross sections of the Airy beam as it propagates along z (second column of Fig. 6). The main lobe width w_0 and its power content P_A are therefore important parameters for characterizing nonlinear Airy beam propagation: We observe from numerical simulations a transition between a regime where the turning ability of the Airy beam is preserved to a regime where nonlinear effects seemingly modify the curvature radius of the Airy peak trajectory due to self-focusing of intense lobes and lobe competition for the available power. This trend is clearly illustrated by the comparison of the second column of Fig. 6 with the first that shows the $I(x,y)$ cross sections of the same Airy beam propagating in air with nonlinear index coefficient n_2 at 1 atm (also shown in the second column of Fig. 2). At high powers, the Airy beam eventually undergoes a reshaping into a multifilamentation pattern with multiple filaments located at the positions of the main secondary lobes of the input Airy beam.

V. PROPAGATION OF TRUNCATED AIRY BEAMS

We identified a second situation of transverse acceleration quenching, that proceeds from the idea of managing the competition between energy fluxes induced by Kerr self-focusing and by peak acceleration. We kept our initial Airy beam parameters $w_0 = 200$ μm, $I_0 = 7 \times 10^{12}$ W/cm^2 and changed the radius of the circular diaphragm. The input Airy beams we considered so far in our simulations were truncated by a circular diaphragm with a rather large radius ($r_d = 4.5$ mm) compared to the main lobe width. This approach makes finite the energy of the input Airy beam while preserving a large number of secondary lobes. Our simulations show that the diaphragm radius has an important effect on the nonlinear propagation of the Airy beam and on its transverse acceleration since the number of secondary lobes controls the energy flux that refills and pushes the main lobe. To facilitate the comparison with previous results, all simulations concerning this topic where conducted for the nonlinear index coefficient n_2 characterizing propagation in air at 10 atm or in water owing to the above-mentioned rescaling.

Figure 7 shows a comparison of the propagation of three Airy beams which have identical main lobe width (200 μm) but which are truncated differently: the diaphragm radius is $r_d = 4.5$ mm in the first column, $r_d = 2.5$ mm in the second column, and $r_d = 1$ mm in the third column of Fig. 7. By using Eq. (5), we obtain Airy zones of 351, 261, and 165 cm which are much larger than the typical distance for self-focusing of the 200-μm-wide lobe containing 26 P_{cr}. The input peak intensity and beam width are the same for all columns of Fig. 7, hence the main lobes of the input Airy beams carry the same power.

In the case of the large apodizer, the linear energy flux of the Airy beam is sustained over a larger propagation distance. The beam truncated by the small diaphragm containing only 3 lobes of the input Airy beam propagates under the action of nonlinear effects over a much shorter distance. The linear energy flux responsible for the curved trajectory is in this case not strong enough to bring energy from the tail to the peak of the Airy beam over the whole Airy zone. The small diaphragm

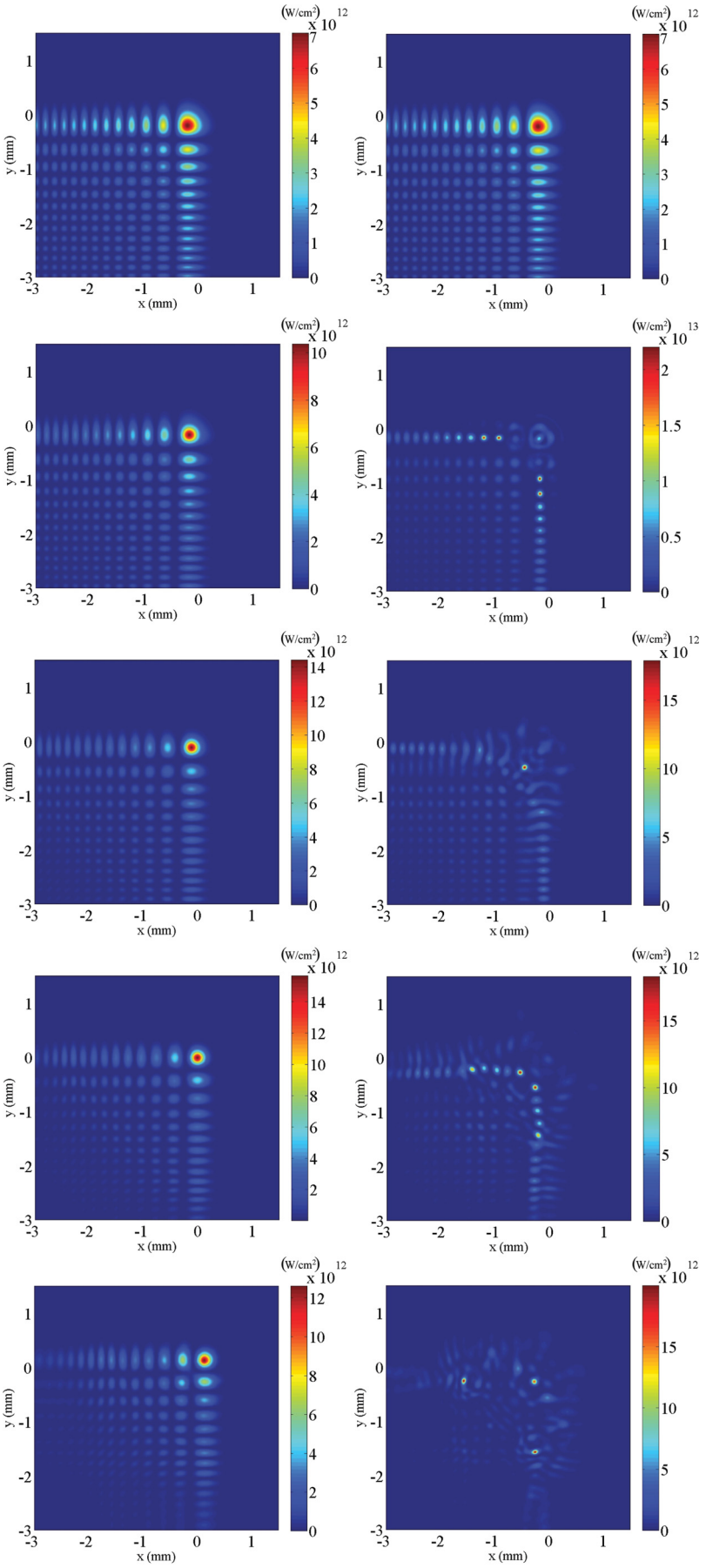

FIG. 6. (Color online) (x, y) intensity plots of nonlinear Airy beams with initial peak intensity 7×10^{12} W/cm^2, with $w_0 = 200$ μm, and a diaphragm of $r_d = 4.5$ mm. First column is $n_2 = 3.2 \times 10^{-19}$ cm^2/W (moderate power regime). Second column is for $n_2 = 3.2 \times 10^{-18}$ cm^2/W (high-power regime). The propagation distance varies from $z = 0$ (first line) to $z = 80$ cm (fifth line) by steps of 20 cm.

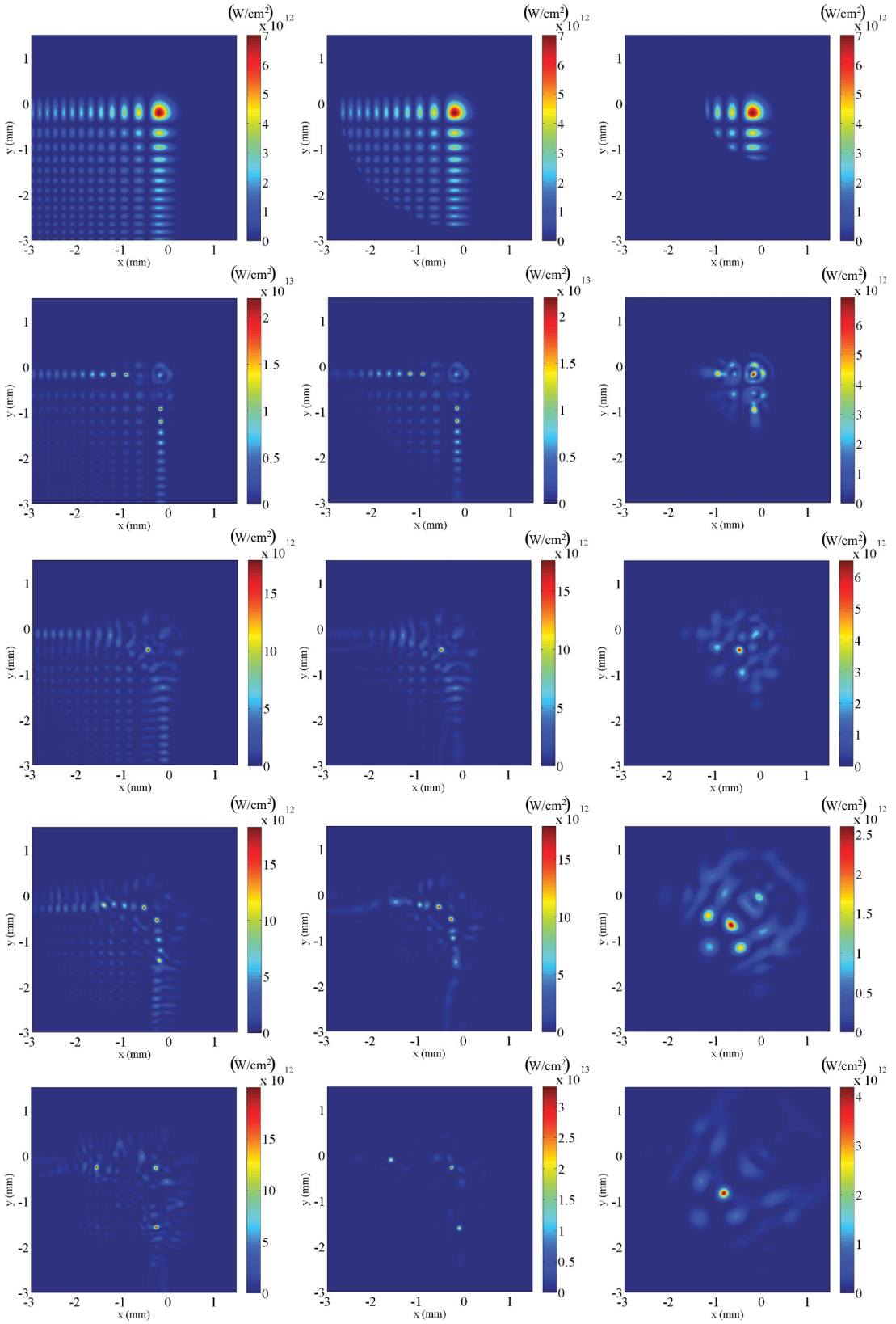

FIG. 7. (Color online) Effect of truncation in high-power regime. The three columns correspond to the propagation of of nonlinear Airy beams with initial peak intensity 7×10^{12} W/cm^2, central lobe size $w_0 = 200$ μm, diaphragmed by circular apertures of radius $r_d = 4.5$ mm (first column), $r_d = 2.5$ mm (second column), and $r_d = 1$ mm (third column), with nonlinear-index coefficient $n_2 = 3.2 \times 10^{-18}$ cm^2/W. The propagation distance varies from $z = 0$ (first line) to $z = 80$ cm (fifth line) by steps of 20 cm.

quenches the power refilling of the secondary lobes and therefore simultaneously tends to quench the turning ability of the Airy beam. Secondary lobes still undergo self-focusing and form filaments, but they subsequently follow a standard filament interaction process featured by energy exchange with the neighborhood. Their intensity increases until multiphoton absorption becomes efficient and plasma is generated that eventually participates in beam spreading and nucleation of other filaments from the reservoir. Figure 7 shows that, although these multiple filaments are initiated at the same locations regardless of the diaphragm size, the smaller the diaphragm radius the earlier in their propagation they depart from each other. In this case the nonlinear dynamics dominate and seemingly prevent the main lobe to turn. In fact, these nonlinear dynamics require a much shorter distance than the Airy zone, thus the associated energy flux is used to fill the secondary lobes of the Airy beam rather than to induce a curvature of the trajectory of the main lobe. So effectively, the diaphragm radius allows us to switch off the energy flux at a given distance.

Nonlinear Airy beam propagation falls into two separate regimes identified on Figs. 6 and 7, depending on whether the linear acceleration and beam profile is preserved. In the strongly nonlinear regime (i.e., for a large relative strength of the self-focusing nonlinearity), the input Airy beam is effectively destroyed during its propagation. This is clearly demonstrated in Fig. 7 at $z = 40$ cm (3rd row) for all three apodizers. In the weakly nonlinear regime, the linear dynamics prevails and the parabolic trajectory of the Airy peak is unperturbed. The strongly nonlinear regime, however, may show manifestations of linear dynamics such as the self-healing property reported in Ref. [10], where part of a linearly propagating Airy beam profile was obscured and observed to be reconstructed after a few cm. The first column of Fig. 7 shows this effect (i.e., the destroyed profile at $z = 40$ cm is partially reconstructed at $z = 60$ cm). At this point multiphoton absorption becomes strong enough to gradually destroy once again the beam profile, as we can see at $z = 80$ cm. The outcome of this competition is actually controlled by the size of the apodizer. As the apodizer size is reduced to $r_d = 2.5$ mm, the reconstruction ability of the Airy beam is weakened, as can be seen in the second column of Fig. 7. In the third case (third column), where $r_d = 1$ mm, the Kerr effect completely dominates over all linear dynamics and the Airy profile is entirely ruined after the short Airy zone. Note that, in all three cases, the strength of the Kerr effect is unchanged and only the apodizer radius (related to the Airy zone length and the self-healing strength) is modified.

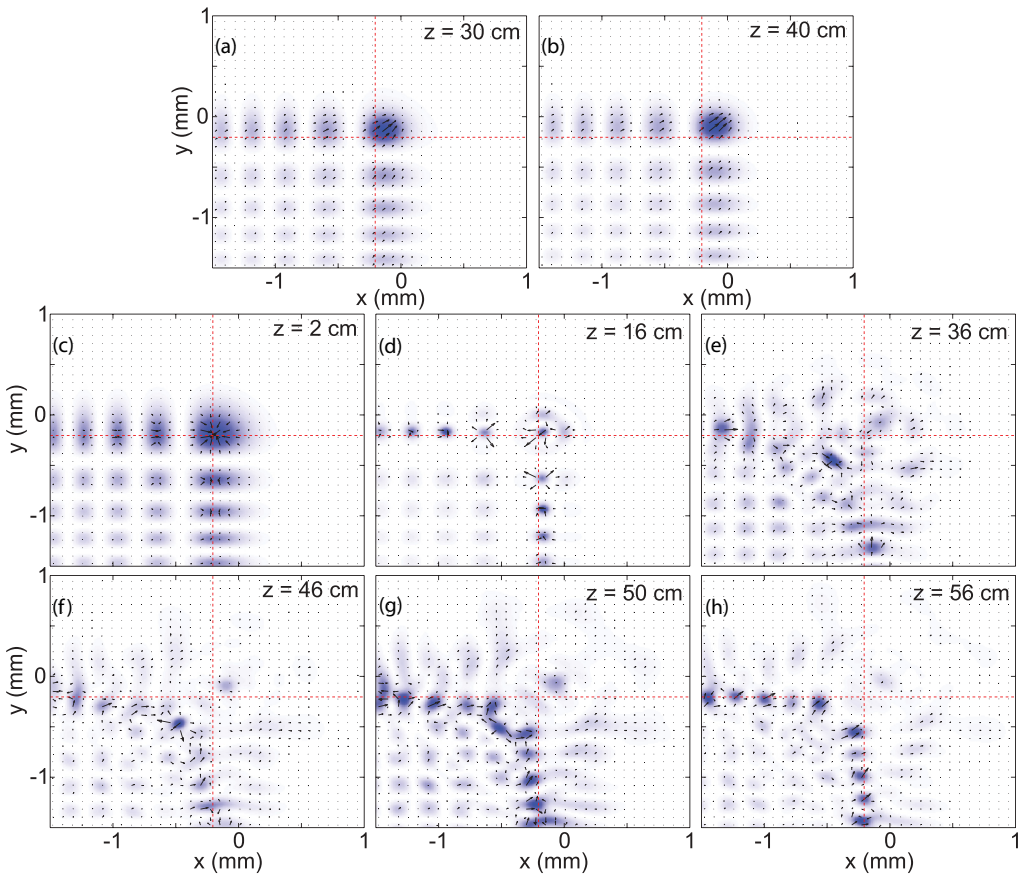

FIG. 8. (Color online) First line shows evolution of energy flux during nonlinear propagation of Airy beams with $w_0 = 200$ μm and moderate power. The arrows indicate the direction of the energy flux while its strength is proportional to arrow lengths. The propagation distances are $z = 30$ and $z = 40$ cm. Second and third lines are same as for the first line but for the high-power regime. The propagation distances are $z = 2$, 16, 36, 46, 50, and 56 cm from left to right and from the second to third line.

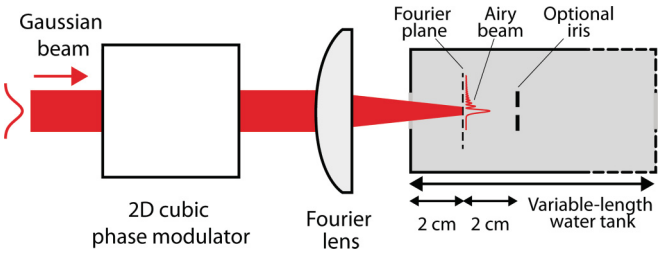

FIG. 9. (Color online) Experimental layout.

VI. ENERGY FLUX ALONG PROPAGATION

Finally, in order to make the dynamics of Airy beam propagation in air more accessible to the reader, we have included movies of the evolution, as a function of the propagation distance z, of the cross section of the intensity $I(x,y)$ superimposed to an arrow plot showing the associated local energy density flux (supplementary material associated with this paper). The transverse components of the energy density flux are simply proportional to the beam intensity and to the phase gradient in the corresponding direction [37–40]. The first movie is associated with the regime of moderate powers [i.e., the propagation of the 200 μm lobe width shown in Fig. 6(a)], while the second is associated with the high-power regime; that is, the propagation of the same input Airy beam in the medium with larger Kerr coefficient used for Fig. 6(b). Figure 8 shows the main features of the energy flux as identified from the movies.

We can observe in the weakly nonlinear regime that the main lobe of the Airy beam is turning because of the energy flux along the symmetry axis $x = y$, from the quadrant ($x < 0$, $y < 0$) toward the peak, as in the case of linear propagation [Figs. 8(a) and 8(b) and first movie [41]].

In the strongly nonlinear regime, we observe that the main Airy lobe undergoes standard filamentation and part of the energy flux from the tail of the Airy beam is feeding the secondary lobes which in turn undergo self-focusing and nonlinear losses. Upon further propagation the main lobe peak decays while one or several of the secondary peaks becomes dominant, until they too decay [Figs. 8(c)–8(g) and second movie [41]]. Visualization of the energy flux allows us to understand the presence of notches in the curve shown in Fig. 5(a), which correspond to propagation distances when a secondary lobe with growing intensity takes over the decaying intensity of the main lobe. Similarly to the scenario for spatial replenishment in filaments [42], a notch in the intensity curve in Fig. 5 is explained as that propagation distance where the increasing secondary peak takes over as the global maximum from the decreasing main lobe peak. This process can repeat itself if the power in the secondary lobe is sufficient to be further transferred to a third-order lobe.

VII. EXPERIMENTAL RESULTS

We performed experiments to observe the moderate- and high-power regimes in Airy beam propagation as well as the effect of Airy beam truncation. As shown in Fig. 9, the laser beam is reshaped into an exponentially apodized 2D Airy beam by using a recently developed technique [4] which exploits coma aberration as a means to imprint a 2D spatial cubic phase onto the initial Gaussian beam followed by spatial Fourier transformation via a spherical lens. The Airy beam is generated at the focus of the Fourier lens, located 2 cm inside a variable-length transparent water tank, where an iris is used to truncate the Airy profile to the desired size. Experiments are performed in water to profit from the higher nonlinearity of the medium.

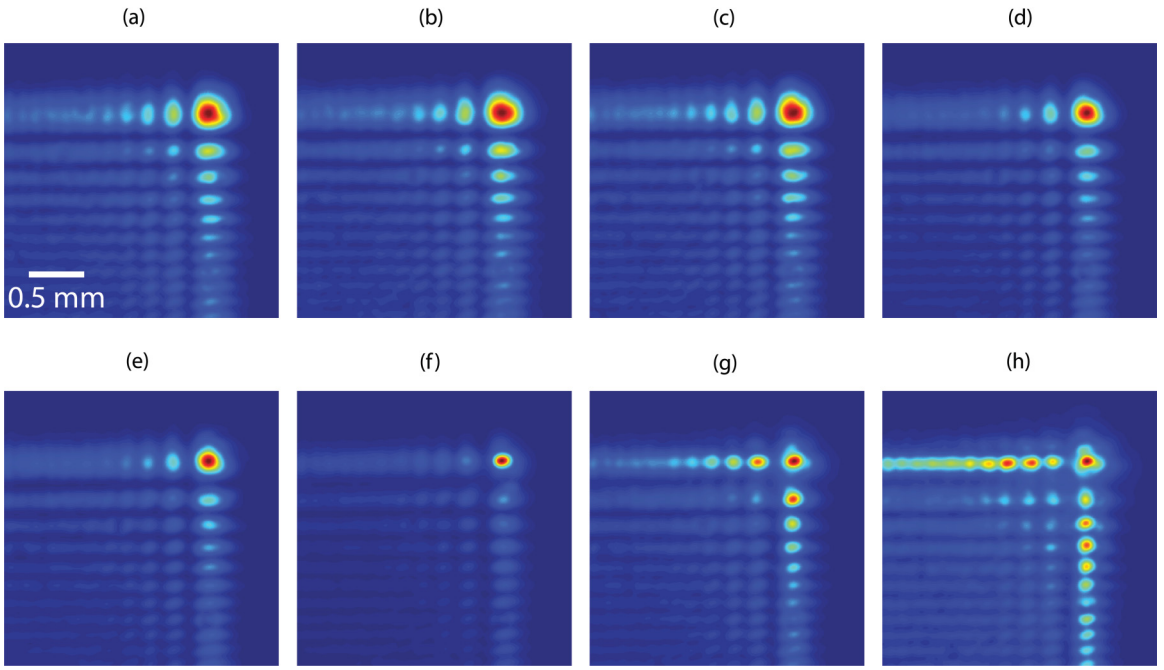

FIG. 10. (Color online) Normalized experimentally measured intensity at $z = 10$ cm after the focus, inside the water tank, for different input pulse energies. (a) 9.5 nJ ($0.03P_{cr}$), (b) 65 nJ ($0.19P_{cr}$), (c) 597 nJ ($1.75P_{cr}$), (d) 2.9 μJ ($8.5P_{cr}$), (e) 5.4 μJ ($16P_{cr}$), (f) 7.5 μJ ($22P_{cr}$), (g) 15 μJ ($44P_{cr}$), (h) 32 μJ ($94P_{cr}$). $w_0 \sim 140$ μm (FWHM 230 μm).

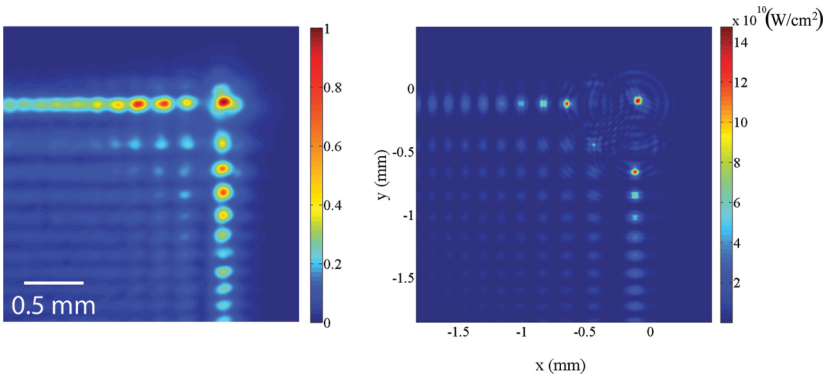

FIG. 11. (Color online) Comparison of nonlinear dynamics between experiments and simulations. Left shows normalized experimentally measured intensity at $z = 10$ cm after the focus inside the water tank, for the highest power ($94P_{cr}$) and $w_0 = 140$ μm. Right shows simulated intensity distribution with identical input conditions after propagation of 10 cm in water.

Figure 10 shows the experimentally generated Airy beam with main lobe FWHM of 230 μm, which corresponds to $w_0 \simeq 140$ μm (Fourier lens $f = 50$ cm), after propagation over 10 cm in water, for 8 different input energies. The 800 nm laser pulse duration where the Airy beams are generated is 80 fs (as the initial pulse of 35 fs goes through a number of dispersive optical elements). The power contained in the Airy profile, at the point of creation inside the water tank, is increased from $0.03P_{cr}$ ($9.5\,nJ$), which is essentially linear, up to $94P_{cr}$ (32 μJ). These values refer to the power contained in the whole Airy beam profile and not only in the main lobe, since the latter is difficult to accurately measure experimentally. However, from previous studies [4,8] the power content of the main lobe can be estimated around 7% of the whole beam, and thus the cases for the highest energy are well inside the high-power regime. As the energy of the pulse is increasing, nonlinear dynamics start to act on the beam shape in the same way as predicted by simulations. Self-focusing of the main Airy lobe clearly occurred for $22P_{cr}$ (total beam). As the beam energy is increased further, secondary lobes start to self-focus and increase in intensity, showing exactly the same trend as predicted by numerical simulations.

In Fig. 11, a close-up of the measured Airy beam profile at $94P_{cr}$ is shown side by side with the simulated intensity

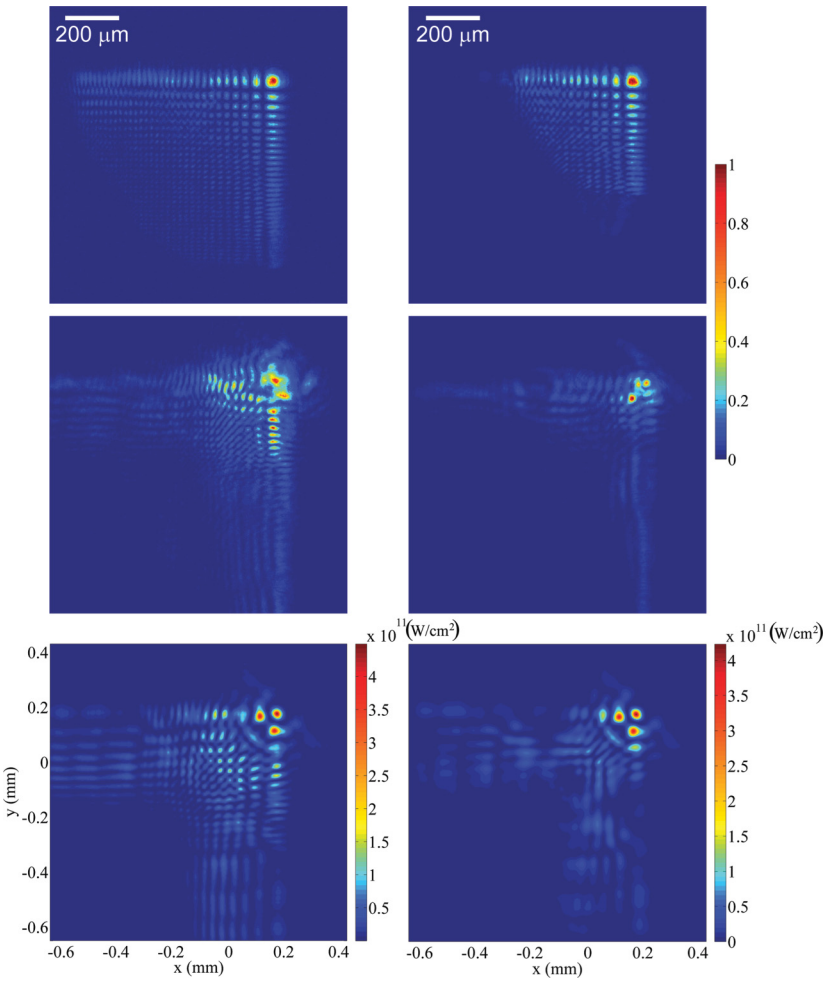

FIG. 12. (Color online) Truncation effect for two different apodizers. First line shows normalized experimental input beams. The apodizers used are $r_d = 750$ μm (left) and $r_d = 450$ μm (right), the main lobe FWHM is $w_0 = 30$ μm. Input powers are $35P_{cr}$ (left) and $20P_{cr}$ (right). Second line is normalized experimental intensity profiles after $z = 4.6$ cm of propagation inside the water tank, for the same pulses as in line one. Last line is simulated intensity profiles at the same position as in line two for identical input conditions.

profile of the truncated ideal Airy beam. The input parameters of the simulated Airy beam are matching the ones of the experiment. Since the code operates in frozen time we take an average pulse duration of 160 fs inside the water tank (due to the dispersion of water). In the simulation, the Airy beam propagates in 10 cm of water with $n_2 = 1.6 \times 10^{-16}$ cm^2/W, which corresponds to $P_{cr} \simeq 4$ MW at the laser wavelength of 800 nm [25]. The ionization coefficients used for water are $\sigma_K = 1 \times 10^{-54}$ s^{-1} cm^{10}/W^5 for $K = 5$ photons, and neutral atom density $\rho_{nt} = 6.6 \times 10^{22}$ cm^{-3} [28]. As we can see in Fig. 11, the measured and the calculated patterns agree very well. In both cases the main lobe is starting to generate a filament-like structure with an extended reservoir around it. The nearby secondary lobes are strongly perturbed, while the subsequent ones are self-focusing and gaining intensity. Beyond the 6th lobe, the beam shape remains unchanged.

We also studied the effect, previously shown in simulations, of Airy beam truncation on nonlinear propagation. Figure 12 shows a comparison between measurements and simulations of two input Airy beams truncated by two different-radius irises. The first line shows the two initial Airy beams used in the experiment. The main lobe size is $w_0 = 30$ μm (Fourier lens $f = 10$ cm) and the apodizer radius is 750 μm (left) and 450 μm (right). The power contained in the two Airy beams is $35P_{cr}$ and $20P_{cr}$ for the large and small apodizer, respectively. After nonlinear propagation over 4.6 cm in water the beams are reshaped as can be seen in the second line of the same figure. In the case of the large iris, some features of the Airy profile are preserved while the most intense first and nearby secondary lobes show manifestations of filamentation. In the case of the small iris, the Airy profile is almost completely destroyed by the nonlinear dynamics, and a multifilamentary pattern is formed in its place. These experimental observations are in very good agreement with corresponding simulation results shown in the third line of Fig. 12.

VIII. CONCLUSION

We have investigated numerically and experimentally the nonlinear dynamics of intense finite energy Airy beams. Nonlinear propagation of Airy beams is found to be governed by the same principles that rules propagation of nonlinear Bessel beams: two regimes are distinguished by the power content of the most intense Airy lobe. At moderate powers, Airy beams propagate smoothly without exhibiting an abrupt increase of intensity that would define a nonlinear focus, even if the power carried by the main lobe is several times above the critical power for self-focusing. The peak intensity does not reach a plateau but slowly increases and eventually drops due to finite size, truncation or apodization effects. The Airy peak is transversely accelerated as in the linear regime. In the high-power regime, the nonlinear dynamics is no longer smooth. The competition between the Kerr effect and the transverse energy flux regulated by the cubic spatial phase of the beam leads to an unsteady propagation featured by the formation and interaction of multiple filaments. If the Kerr effect dominates, multiple lobes will indeed self-focus on themselves and form filaments. This procedure leads to a destruction of the Airy beam profile and as a result the turning ability is lost. Alternatively, when the linear transverse flux dominates, the beam tends to accelerate along the diagonal, even though individual lobe shrinking (due to self-focusing) is still observed. This competition can be observed over an Airy zone, the length of which is determined by apodization or truncation effects. These results apply to transparent media in general: gases liquids or solids and might be useful for engineering optical materials with Airy beams [43].

ACKNOWLEDGMENT

This work was supported by the European Union Marie Curie Excellence Grant MULTIRAD MEXT-CT-2006-042683.

[1] G. A. Siviloglou and D. Christodoulides, Opt. Lett. **32**, 979 (2007).
[2] G. A. Siviloglou, J. Broky, A. Dogariu, and D. N. Christodoulides, Phys. Rev. Lett. **99**, 213901 (2007).
[3] M. V. Berry and N. L. Balazs, Am. J. Phys. **47**, 264 (1979).
[4] D. G. Papazoglou, S. Suntsov, D. Abdollahpour, and S. Tzortzakis, Phys. Rev. A **81**, 061807(R) (2010).
[5] D. M. Cottrell, J. A. Davis, and T. M. Hazard, Opt. Lett. **34**, 2635 (2009).
[6] J. A. Davis, M. J. Mitry, M. A. Bandres, I. Ruiz, K. P. McAuley, and D. M. Cottrell, Appl. Opt. **48**, 3170 (2009).
[7] A. Chong, W. H. Renninger, D. N. Christodoulides, and F. W. Wise, Nat. Photonics **4**, 103 (2010).
[8] D. Abdollahpour, S. Suntsov, D. G. Papazoglou, and S. Tzortzakis, Phys. Rev. Lett. **105**, 253901 (2010).
[9] T. Ellenbogen, N. Voloch-Bloch, A. Ganany-Padowicz, and A. Arie, Nat. Photonics **3**, 395 (2009).
[10] J. Broky, G. A. Siviloglou, A. Dogariu, and D. N. Christodoulides, Opt. Express **16**, 12880 (2008).
[11] G. A. Siviloglou, J. Broky, A. Dogariu, and D. N. Christodoulides, Opt. Lett. **33**, 207 (2008).
[12] J. E. Morris, M. Mazilu, J. Baumgartl, T. Cizmar, and K. Dholakia, Opt. Express **17**, 13236 (2009).
[13] I. M. Besieris and A. M. Shaarawi, Phys. Rev. E **78**, 046605 (2008).
[14] J. Parravicini, P. Minzioni, V. Degiorgio, and E. DelRe, Opt. Lett. **34**, 3908 (2009).
[15] P. Polynkin, M. Kolesik, J. V. Moloney, G. A. Siviloglou, and D. N. Christodoulides, Science **324**, 229 (2009).
[16] P. Polynkin, M. Kolesik, and J. Moloney, Phys. Rev. Lett. **103**, 123902 (2009).
[17] A. Lotti, D. Faccio, A. Couairon, D. G. Papazoglou, P. Panagiotopoulos, D. Abdollahpour, and S. Tzortzakis, Phys. Rev. A **84**, 021807(R) (2011).
[18] A. Couairon and A. Mysyrowicz, Phys. Rep. **441**, 47 (2007).
[19] A. Couairon, E. Brambilla, T. Corti, D. Majus, O. de J. Ramirez-Gongora, and M. Kolesik, Eur. Phys. J. Spec. Top. **199**, 5 (2011).

[20] I. Kaminer, M. Segev, and D. N. Christodoulides, Phys. Rev. Lett. **106**, 213903 (2011).
[21] Y. Shimoji, A. T. Fay, R. S. F. Chang, and N. Djeu, J. Opt. Soc. Am. B **6**, 1994 (1989).
[22] E. T. J. Nibbering, G. Grillon, M. A. Franco, B. S. Prade, and A. Mysyrowicz, J. Opt. Soc. Am. B **14**, 650 (1997).
[23] L. V. Keldysh, Sov. Phys. JETP **20**, 1307 (1965) [Zh. Eksp. Teor. Fiz. **47**, 1945 (1964)].
[24] F. A. Ilkov, J. E. Decker, and S. L. Chin, J. Phys. B **25**, 4005 (1992).
[25] W. L. Smith, P. Liu, and N. Bloembergen, Phys. Rev. A **15**, 2396 (1977).
[26] S. Minardi, A. Gopal, M. Tatarakis, A. Couairon, G. Tamosauskas, R. Piskarskas, A. Dubietis, and P. Di Trapani, Opt. Lett. **33**, 86 (2008).
[27] S. Minardi, A. Gopal, A. Couairon, G. Tamosauskas, R. Piskarskas, A. Dubietis, and P. Di Trapani, Opt. Lett. **34**, 3020 (2009).
[28] P. K. Kennedy, S. A. Boppart, D. X. Hammer, B. A. Rockwell, G. D. Noojin, and W. P. Roach, IEEE J. Quantum Electron. **31**, 2241 (1995).
[29] P. Panagiotopoulos, A. Couairon, N. K. Efremidis, D. G. Papazoglou, and S. Tzortzakis, Opt. Express **19**, 10057 (2011).
[30] A. G. Van Engen, S. A. Diddams, and T. S. Clement, Appl. Opt. **37**, 5679 (1998).
[31] A. Couairon, S. Tzortzakis, L. Bergé, M. Franco, B. Prade, and A. Mysyrowicz, J. Opt. Soc. Am. B **19**, 1117 (2002).
[32] J. C. Diels, J. Yeak, D. Mirell, R. Fuentes, S. Rostami, D. Faccio, and P. Di Trapani, Laser Phys. **20**, 1101 (2010).
[33] P. Polesana, A. Couairon, D. Faccio, A. Parola, M. A. Porras, A. Dubietis, A. Piskarskas, and P. Di Trapani, Phys. Rev. Lett. **99**, 223902 (2007).
[34] J. Broky, G. A. Siviloglou, A. Dogariu, and D. N. Christodoulides, Opt. Express **16**, 12880 (2008).
[35] A. Couairon, H. S. Chakraborty, and M. B. Gaarde, Phys. Rev. A **77**, 053814 (2008).
[36] A. Couairon, Phys. Rev. A **68**, 015801 (2003).
[37] P. Polesana, M. Franco, A. Couairon, D. Faccio, and P. Di Trapani, Phys. Rev. A **77**, 043814 (2008).
[38] D. Faccio, A. Lotti, A. Matijosius, F. Bragheri, V. Degiorgio, A. Couairon, and P. Di Trapani, Opt. Express **17**, 8193 (2009).
[39] A. Lotti, A. Couairon, D. Faccio, and P. Di Trapani, Phys. Rev. A **81**, 023810 (2010).
[40] D. Faccio, A. Averchi, A. Lotti, P. Di Trapani, A. Couairon, D. Papazoglou, and S. Tzortzakis, Opt. Express **16**, 1565 (2008).
[41] See Supplemental Material at http://link.aps.org/supplemental/10.1103/PhysRevA.86.013842 for movies.
[42] M. Mlejnek, E. M. Wright, and J. V. Moloney, Opt. Express **4**, 223 (1999).
[43] L. Froehly, F. Courvoisier, A. Mathis, M. Jacquot, L. Furfaro, R. Giust, P. A. Lacourt, and J. M. Dudley, Opt. Express **19**, 16455 (2011).